The Astrophysical Journal Letters, 892:L19 (8pp), 2020 April 1 https://doi.org/10.3847/2041-8213/ab7fb2

Planet-induced Vortices with Dust Coagulation in Protoplanetary Disks

Ya-Ping Li (李亚平)[1], Hui Li (李晖)[1], Shengtai Li (李胜台)[1], Tilman Birnstiel[2,3], Joanna Drążkowska[2], and Sebastian Stammler[2]
[1] Theoretical Division, Los Alamos National Laboratory, Los Alamos, NM 87545, USA; leeyp2009@gmail.com
[2] University Observatory, Faculty of Physics, Ludwig-Maximilians-Universität München, Scheinerstr. 1, D-81679 Munich, Germany
[3] Exzellenzcluster ORIGINS, Boltzmannstr. 2, D-85748 Garching, Germany
Received 2020 January 10; revised 2020 March 5; accepted 2020 March 13; published 2020 March 31

Abstract

In this work, we study how the dust coagulation/fragmentation will influence the evolution and observational appearances of vortices induced by a massive planet embedded in a low-viscosity disk by performing global 2D high-resolution hydrodynamical simulations. Within the vortex, due to its higher gas surface density and steeper pressure gradients, dust coagulation, fragmentation, and drift (to the vortex center) are all quite efficient, producing dust particles ranging from 1 μm to $\sim$1.0 cm, as well as an overall high dust-to-gas ratio (above unity). In addition, the dust size distribution is quite nonuniform inside the vortex, with the mass-weighted average dust size at the vortex center ($\sim$4.0 mm) being a factor of $\sim$10 larger than other vortex regions. Both large ($\sim$millimeter) and small (tens of microns) particles contribute strongly to affect the gas motion within the vortex. As such, we find that the inclusion of dust coagulation has a significant impact on the vortex lifetime and the typical vortex lifetime is about 1000 orbits. After the initial gaseous vortex is destroyed, the dust spreads into a ring with a few remaining smaller gaseous vortices with a high dust concentration and a large maximum size ($\sim$millimeter). At late time, the synthetic dust continuum images for the coagulation case show as a ring inlaid with several hot spots at the 1.33 mm band, while only distinct hot spots remain at 7.0 mm.

Unified Astronomy Thesaurus concepts: Exoplanets (498); Protoplanetary disks (1300); Planet formation (1241); Dust continuum emission (412); Gas-to-dust ratio (638); Hydrodynamical simulations (767)

1. Introduction

Vortices in protoplanetary disks may play essential roles in the early stage of planet formation due to their effectiveness in trapping dust, which could be an ideal place to trigger planetesimal formation (Barge & Sommeria 1995; Zhu et al. 2012; Birnstiel et al. 2013; Casassus et al. 2013; Meheut et al. 2013; Zhu & Stone 2014). These vortices appeared as lopsided horseshoes, or crescent asymmetric features have been observed by several (sub)millimeter observations, e.g., IRS 48 (van der Marel et al. 2013), LkHα 330 (Isella et al. 2013), HD 142527 (Muto et al. 2015), MWC 758 (Isella et al. 2010), AB Aur (Fuente et al. 2017), SR 21 (Pérez et al. 2014), and SAO 206462 (Pérez et al. 2014). These observed sub-structures can be formed by the Rossby wave instability (RWI; Lovelace et al. 1999; Li et al. 2000, 2001; Ono et al. 2018) at the edges of a gap opened by a massive planet embedded in a low-viscosity disk (Li et al. 2005; Huang et al. 2018), at the edges of the accretionally inactive dead zones (Miranda et al. 2017; Regály & Vorobyov 2017), by a binary companion without generating vortices (Calcino et al. 2019), or by the baroclinic instability (Klahr & Bodenheimer 2003; Raettig et al. 2013; Lyra 2014).

The long-term evolution of vortices has been studied by Fu et al. (2014a), which suggests that a low gas viscosity is required to sustain vortices to thousands and up to 10^4 orbits (see also de Val-Borro et al. 2007; Hammer et al. 2017). Fu et al. (2014b) further found that the feedback effect from the dust (the back reaction of dust onto gas) in 2D simulations can reduce the lifetime of the vortices by a factor of up to 10 for a variety of initial dust-to-gas ratios and single dust particle sizes. It has also been found that vortices in 3D disks are subject to "elliptic instability," which reduces the viability of these vortices as dust traps (Lesur & Papaloizou 2009; Lithwick 2009; Barge et al. 2016; Lin & Pierens 2018). However, the dust size growth during the whole evolution of the disk, which was implemented only recently in the global 2D disk model (Drążkowska et al. 2019; Laune et al. 2020), has not been considered for all these studies. Drążkowska et al. (2019) studied the dust distribution in the vicinity of a Jupiter-mass planet embedded in a relatively high viscosity disk, while Laune et al. (2020) explored the ring morphology affected by coagulation in the parameter regime of a low viscosity and a low planet mass.

As the dust feedback becomes important when the dust-to-gas ratio approaches unity, which increases with time in the vortex region due to the radial drift and collecting process. Both of these processes become faster with a larger Stokes number (i.e., $\propto \mathrm{St}^{-1}$; St is defined in Equation (3)) or a larger dust size in the small Stokes number regime, although the collecting process is much faster than the radial drift (Surville et al. 2016). Therefore, the coagulation, which controls the dust size growth, can play an important role in controlling the efficiency of dust feedback. The fragmentation, however, distributes the surface density from large particles into small ones, thus the increase of the dust-to-gas ratio cannot be so efficient compared with the single-species model. The efficiency of dust feedback, and then the evolution of large-scale vortices, thus results from the complex interplay between the dust coagulation/fragmentation and radial drift. Here we include the dust coagulation/fragmentation to study its effect on the evolution of planet-induced vortices and observational appearances in protoplanetary disks.

The rest of the Letter is organized as follows. Our coagulation and single-species models are described in Section 2. We then present the results and discuss the

observational implications in Section 3, and we conclude in Section 4.

2. Methods

Similar to Drążkowska et al. (2019) and Laune et al. (2020), where they explored different regimes of planet mass or viscosity, we study the effect of coagulation on the vortex evolution induced by a massive planet embedded in a low-viscosity protoplanetary disk. As inferred from observations for IRS 48 (van der Marel et al. 2013), a $5\,M_J$ (where M_J is the Jupiter mass) planet is assumed to orbit a $2M_\odot$ (where $M_\odot$ is the solar mass) star on a fixed circular orbit at a radius of 20 au. A low-viscosity parameter $\alpha_{\rm vis} = 7 \times 10^{-5}$ throughout the disk is adopted to sustain the gaseous vortex (Fu et al. 2014a). We assume an α-prescription for the gas kinematic viscosity $\nu_g = \alpha_{\rm vis} c_s h_g$ (Shakura & Sunyaev 1973).

We choose an exponential decay profile for the initial gas surface density $\Sigma_g(r)$ as

$$\Sigma_g(r) = \Sigma_0 \left(\frac{r}{r_c}\right)^{-\gamma} \exp\left[-\left(\frac{r}{r_c}\right)^{2-\gamma}\right], \quad (1)$$

where $r_c = 80$ au and $\gamma = 0.8$. The normalization of gas surface density $\Sigma_0 = 1.3$ g cm^{-2}. The disk extends from 8 to 320 au. Disk self-gravity in gas and dust is not included due to a low disk mass of $M_{\rm disk} = 4.5 \times 10^{-3}\,M_\odot$ or, equivalently, a large minimum Toomre Q parameter across the disk $\sim$150 initially, as suggested by previous works (Lovelace & Hohlfeld 2013; Zhu & Baruteau 2016). The locally isothermal sound speed c_s is chosen as $\frac{c_s}{v_K} = \frac{h_g}{r} = h_0\left(\frac{r}{r_0}\right)^{0.25}$, where $v_K(r)$ is the local Keplerian speed, $r_0 = 20$ au, and $h_0 = 0.06$. This corresponds to a disk temperature profile as $T = 89.0(r/r_0)^{-0.5}$ K. We adopt an isothermal equation of state $P = c_s^2 \Sigma_g$ for the gas component, where P is the vertically integrated gas pressure. The gas and dust fluids for the coagulation model are evolved following the conservation of mass, radial, and angular momentum equations (Li et al. 2019b).

The dust feedback, i.e., drag forces between the gas and dust, are incorporated into the momentum equation for both the gas and dust (Fu et al. 2014b). The drag force f_d^i for a dust species with its size a^i is defined as

$$\boldsymbol{f}_d^i = \frac{\Omega_K}{{\rm St}^i}(\boldsymbol{v}_g - \boldsymbol{v}_d^i), \quad (2)$$

where Ω_K is the Keplerian angular velocity. ${\rm St}^i$ and $\boldsymbol{v}_d^i$ are the Stokes number and dust velocity for species i, respectively. $\boldsymbol{v}_g$ is the gas fluid velocity. We have included Epstein and Stokes regimes for the aerodynamic drag between gas and dust. In the Epstein regime for most regions of the disk, the Stokes number of the particle with a dust radius a in the midplane of the disk is defined as

$${\rm St} = \frac{\pi \rho_s a}{2\Sigma_g}, \quad (3)$$

where $\rho_s = 0.8$ g cm^{-3} is the internal density of the dust particles. For our disk parameters, ${\rm St}(r_0) = 0.16$ with a dust size of 4.0 mm. The dust size corresponding to a unity Stokes number is $a_{{\rm St}=1} = \frac{2\Sigma_g}{\pi\rho_s}$, which is 2.4 cm at 20 au for our initial gas profile.

To understand how the feedback force influences the dust evolution, we adopt the approach of Takeuchi & Lin (2002) to examine its dependence on St before the back reaction becomes important for the gas dynamics. The radial velocity of the dust is

$$v_{d,r} = \frac{v_{g,r} + 2{\rm St}\Delta v_{g,\phi}}{1 + {\rm St}^2}, \quad (4)$$

where $\Delta v_{g,\phi} = v_{g,\phi} - v_K \simeq -1/2\eta v_K$; the second equality applies when $\eta \ll 1$, where $\eta = -\frac{c_s^2}{v_K^2}\frac{d\log P}{d\log r}$, and

$$v_{g,r} = -\frac{3}{\Sigma_g \sqrt{r}}\frac{\partial}{\partial r}(\Sigma_g \nu_g \sqrt{r}) \quad (5)$$

is the radial velocity of the gas when there is no dust back reaction, which is on the order of $\sim\alpha_{\rm vis}(c_s/v_K)^2 v_K$. When ${\rm St} \ll 1$, the radial velocity of dust is reduced to $v_{d,r} \simeq v_{g,r} + 2\Delta v_{g,\phi}{\rm St}$. The radial force is then expressed as

$$f_{d,r} = \frac{{\rm St} v_{g,r} - 2\Delta v_{g,\phi}}{{\rm St}^2 + 1}\Omega_K. \quad (6)$$

When ${\rm St} \ll 1$, $f_{d,r} \simeq -2\Delta v_{g,\phi}\Omega_K$ is independent on St. We find that $f_{d,r}$ usually dominates over $f_{d,\phi}$ if ${\rm St} \lesssim 1$. The effective drag force exerted on gas from each species is then $\boldsymbol{F}_d^i = \boldsymbol{f}_d^i \Sigma_d^i/\Sigma_g$ for each species, where Σ_d^i is the dust surface density (Fu et al. 2014b; Li et al. 2019b). The total drag force $\boldsymbol{F}_d$ for all dust species $\boldsymbol{F}_d^i$ is the summation of $\boldsymbol{F}_d^i$ over i if multiple dust species are included. This value can be significant if the pressure gradient parameter η in the vortex region becomes large, and $\boldsymbol{F}_d$ can be comparable to pressure forces $(1/\Sigma_g)dP/dr$ if $\Sigma_d/\Sigma_g \sim 1$.

We run four models to quantify the effect of coagulation on the vortex evolution. One includes 2D coagulation, and the other two are for a single dust species. For the coagulation run, the details have been described in Li et al. (2019b), Drążkowska et al. (2019), and Laune et al. (2020). Only 1.0 μm sized dust particles are included in the disk initially. The dust size distribution is resolved with 151 dust species covering sizes between 1.0 μm and 100 cm. Collisional outcomes include sticking (fragmentation) when impact speeds for collisions are below (above) a critical speed of $v_f = 10$ m s^{-1}. Due to the computational expense of dust coagulation, we implement a substepping routine and call the coagulation solver every 50 hydro time steps.[4] We use a turbulence parameter $\alpha_t = 10^{-3}$ for the dust coagulation/fragmentation, which is different from the gas viscosity $\alpha_{\rm vis}$ (Carrera et al. 2017). In most cases, we should expect that $\alpha_t < \alpha_{\rm vis}$, where the turbulence that stirs dust can also induce gas accretion. One main reason for adopting $\alpha_t > \alpha_{\rm vis}$ here is that we need a low $\alpha_{\rm vis}$ to trigger RWI for vortex formation, while a larger α_t can avoid an extremely large dust size due to coagulation. Another possibility is that the midplane α_t could

[4] Due to the existence of asymmetric features, we have tested the coagulation model with 25 hydro time steps using a low resolution (1024 × 1024), and find that it can slightly speed up the destruction of the large-scale vortex. But note that in our high-resolution run, the hydro step is much smaller and 50 hydro steps correspond to 0.02 orbit, which can resolve the fine structures within the vortex. We, therefore, expect this substepping does not change our results significantly.

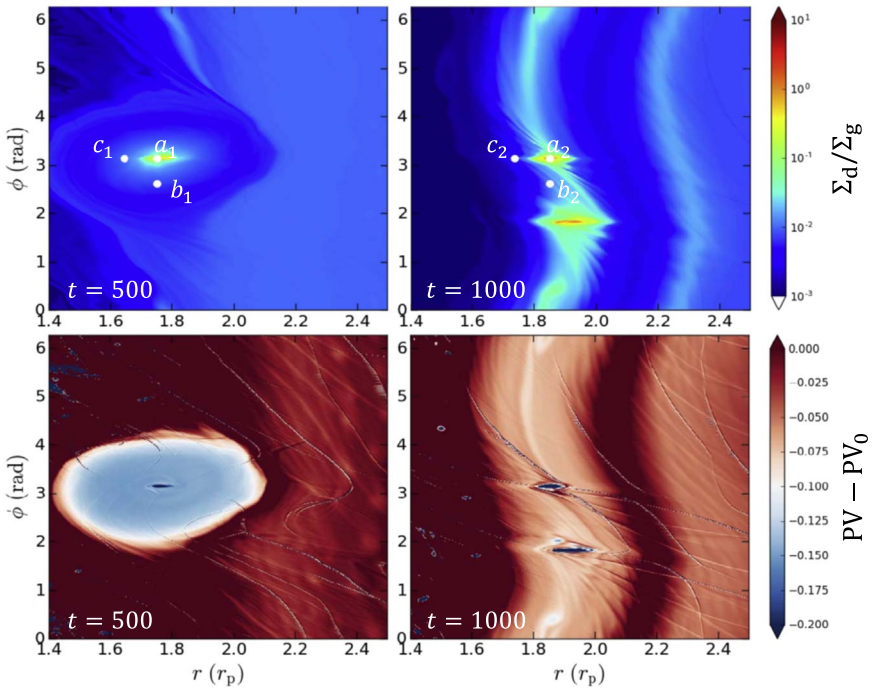

Figure 1. Gas and dust dynamics around the gaseous vortex region for the coagulation run. Upper panels: total Σ_d/Σ_g for all dust species at 500 (left) and 1000 (right) orbits. Lower panels: PV subtracted from the initial value at 500 (left) and 1000 (right) orbits.

be determined by the local instability (e.g., vertical shear instability), while α_{vis} controls the *global* viscosity for the disk accretion, which can be determined by other MHD processes (e.g., Bai & Stone 2013). The dust turbulence parameter $\alpha_t = 10^{-3}$ we adopt is close to the inferred value from observations (Flaherty et al. 2017). The region with a smaller α_{vis} could correspond to the viscously inactive zone, where the vortex tends to be formed, while the disk global viscous evolution for the region far from the vortex, even with a larger $\alpha_{vis} \sim 10^{-2}$, should be unaffected within a timescale of ~1000 orbits.

For the run with a single dust species, we have two runs with the dust size fixed at $a = 4.0$ mm or $a = 0.2$ mm. The size $a = 4.0$ mm is close to the Σ_d-weighted dust size during the evolution of our coagulation model, while $a = 0.2$ mm is the commonly used dust size for the single-species run. For all cases, the surface density distribution of dust follows the radial profile of the gas with an initial radial-independent dust-to-gas mass ratio of 0.01 at the initial stage. To mimic the coagulation run, we also have another run with five species of dust logarithmically uniform spaced between 1.0 μm and 4.0 mm with an initial Mathis Rumpl Nordsieck (MRN) distribution (Mathis et al. 1977) to examine the long-term evolution behavior. Note that dust coagulation/fragmentation is not considered for this model.

We solve the 2D hydrodynamics equations with LA-COMPASS (Li et al. 2005, 2009, 2019b; Fu et al. 2014b) in a logarithmically radial grid of $n_r = 4096$, and a uniform azimuthal grid of $n_\phi = 3456$. With a such high resolution to capture the vortex structures (Fu et al. 2014b), the coagulation run is quite computationally expensive. Specifically, it takes about 1 million CPU hours for our coagulation model, which makes a parameter study unrealistic. We keep the gas density constant at the inner and outer boundaries. An outflow boundary condition is imposed on the dust inner/outer boundary (Drążkowska et al. 2019; Li et al. 2019a).

3. Results

3.1. Coagulation Model

We first show the gas and dust dynamics of the coagulation model. The massive planet can quickly carve out a clean gap around the planet location. The outer edge of the gap ($r \sim 1.8$) becomes Rossby wave unstable. The multiple vortices produced at the early stage quickly merge into a large-scale gaseous vortex, which can be seen from the snapshot for gas potential vorticity (PV; PV $= (\nabla \times \boldsymbol{v}_g)/\Sigma_g$) at $t = 500$ orbits. The PV contours subtracted from its initial value are shown in the lower panels of Figure 1. At $t = 500$, PV is still relatively smooth with a minimum at the vortex center.

As the particles drift from the outer region of disk, they will be collected into the vortex region, which is associated with the gas bump. The particles grow in size when accompanied by the drift. Due to the small particle size in the outer region of disk where particles drift inward (i.e., less than 0.2 mm; see the upper panel of Figure 2), only a small fraction of the total dust mass (~17%, or 2.0 $M_\oplus$, where $M_\oplus$ is the Earth mass) can be collected into the vortex region (e.g., the radial band of $r \sim [1.6, 2.0]$). The azimuthal-averaged dust size distribution at 500 orbits is shown in the upper panel of Figure 2. We can see that the dust growth is mainly limited by the fragmentation a_{frag} (Birnstiel et al. 2012; Li et al. 2019b) and radial drift barrier a_{drift} (Birnstiel et al. 2012) calculated using the azimuthal gas surface density profile. At the outer edge of the gap, the maximum dust size can only be a few tens of microns.

The dust mass can then spiral inward into the vortex center. The dust fragmentation and drift barrier in the center is also larger due to the existence of the gas bump, leading to an increase of the maximum dust size to ~1.0 cm while sinking into the center (point a_1, corresponding to the location of the maximum Σ_d) from the edge (points b_1 and c_1) of the vortex, as shown in the middle panel of Figure 2. The size distribution is quite nonuniform inside the vortex, with the Σ_d-weighted dust

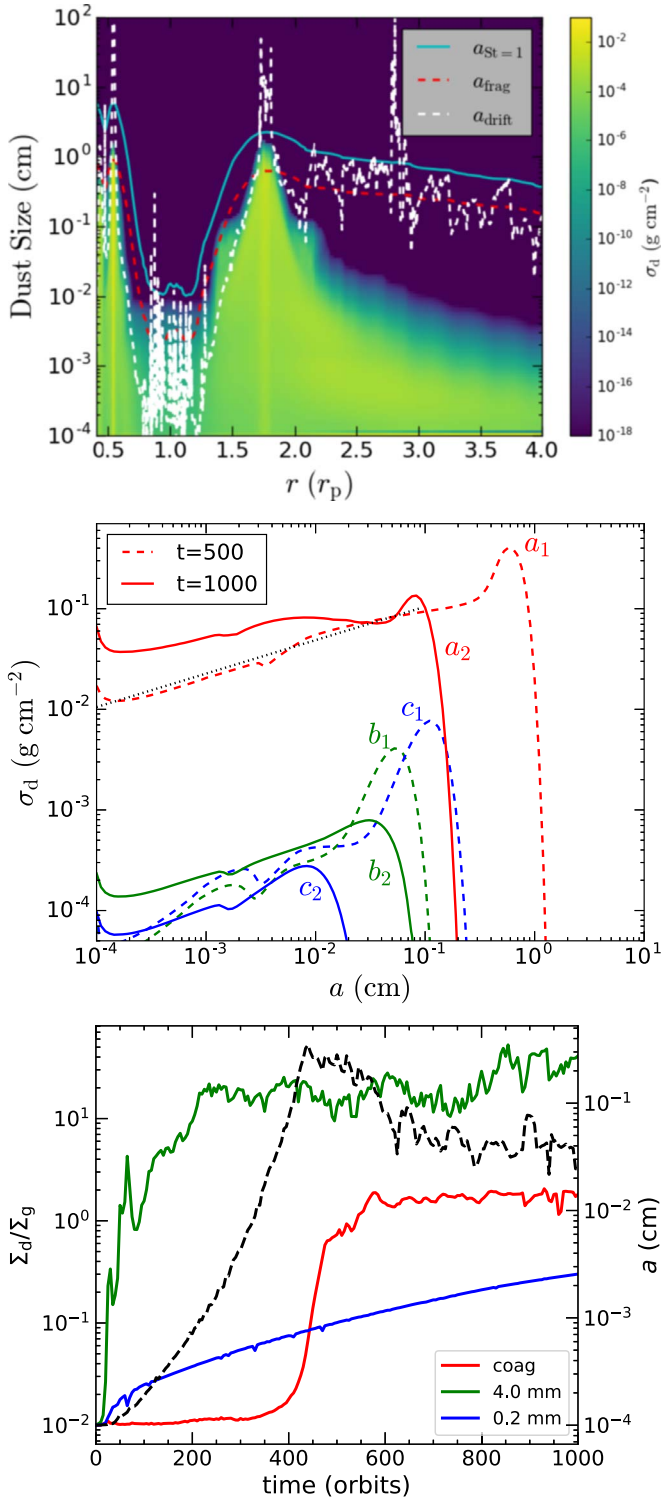

Figure 2. Upper panel: the azimuthal-averaged dust surface density as a function of dust size and radial distance from the star for the time of 500 orbits. Different lines correspond to different size limits. The oscillation of $a_{\rm drift}$ is related to the azimuthal averaging of the wobbling disk. Middle panel: dust surface density as a function of dust size at three locations, which are marked in the upper panels of Figure 1. The black dotted line is a power-law fit to the dashed red line with a slope of 0.33. The red lines correspond to the location of the maximum dust surface density at each time. Bottom panel: the time evolution of the dust-to-gas ratio Σ_d/Σ_g at the vortex center (i.e., the location of maximum Σ_d) for three models (color solid lines). The black dashed line shows the Σ_d-weighted dust size a evolution at the vortex center for the coagulation model.

size at the vortex center (∼4.0 mm) being a factor of ∼10 larger than other vortex regions. The size growth can also speed up the collecting process of the particles due to its dependence on Stokes number (Surville et al. 2016). Therefore, both Σ_d and Σ_d/Σ_g increase rapidly toward the center region. The dust surface density of small particles around the vortex region is also enhanced accompanied by the big ones, as shown by the dashed line in the middle panel of Figure 2, because they are created by fragmenting the big ones. A distinct maximum for Σ_d/Σ_g (or dust surface density) is then formed at the center as shown in the upper left panel of Figure 1 (see also Fu et al. 2014b; Crnkovic-Rubsamen et al. 2015). The scale of the small dust clumps shown in the upper panels of Figure 1 is mainly determined by the dust turbulence diffusivity (Chang & Oishi 2010).

The time evolution of Σ_d/Σ_g is shown in the lower panel of Figure 2, which clearly demonstrates two stages of evolution. The dust grows from the initial size of 1 μm to the maximum value by the time of 400 orbits, which is a factor of two longer than the estimate by Birnstiel et al. (2012) and Laune et al. (2020). Such a discrepancy could be due to the fact that the dust relative velocity is dominated by radial drift rather than turbulence in the outer disk. In this first stage, the increase of Σ_d/Σ_g is quite inefficient due to the small Stokes number. The efficient dust collecting process starts after the dust grows to the maximum size.

As the particle collecting process proceeds, the total dust-to-gas ratio Σ_d/Σ_g is higher than unity in the center of the vortex at 600 orbits and gets saturated afterward, as shown in the lower panel of Figure 2. Such a collecting timescale (∼200 orbits) is roughly consistent with the analytical estimate of ∼170 orbits by Surville et al. (2016, $2\tau_{1/2}$ defined in Equation (38) therein) with an initial Stokes number of 0.01. It is thus the combination of dust size growth and collecting processes that determine that the timescale for the increase of Σ_d/Σ_g to unity, which finally controls the lifetime of the gaseous vortex. The feedback of dust onto gas can trigger the vortex streaming instability (Surville et al. 2016), which produces fluffy "finger" features around the center of the vortex as discovered in Fu et al. (2014b) and Crnkovic-Rubsamen et al. (2015). These fluffy features can result in the elongation in the azimuthal direction, and finally destroys the large-scale vortex due to the "heavy core" instability (Chang & Oishi 2010), which disperses the large-scale vortex into the whole azimuthal domain as seen from the right panels of Figure 1. There exist some substructures in the gas surface density as seen from the PV plot, which can still trap the dust into two bumpy regions. The dust is also stretched into an elongated ring as the PV pattern. The maximum dust size in the PV minimum decreases to a smaller value (∼1.0 mm), as shown in the middle and lower panels of Figure 2, because the gas bump becomes much shallower. A dusty ring is formed after the destruction of the vortex, with the wobbling features related to the very massive planet.

3.2. Comparison with Single-species Models

The effect of dust feedback from the single species on the evolution of the gaseous vortex has been studied by several authors (Fu et al. 2014b; Crnkovic-Rubsamen et al. 2015; Surville et al. 2016). They have shown that a large dust size (equivalently, a large initial Stokes number) can shorten the lifetime of the vortex. Here we mainly use these single-species

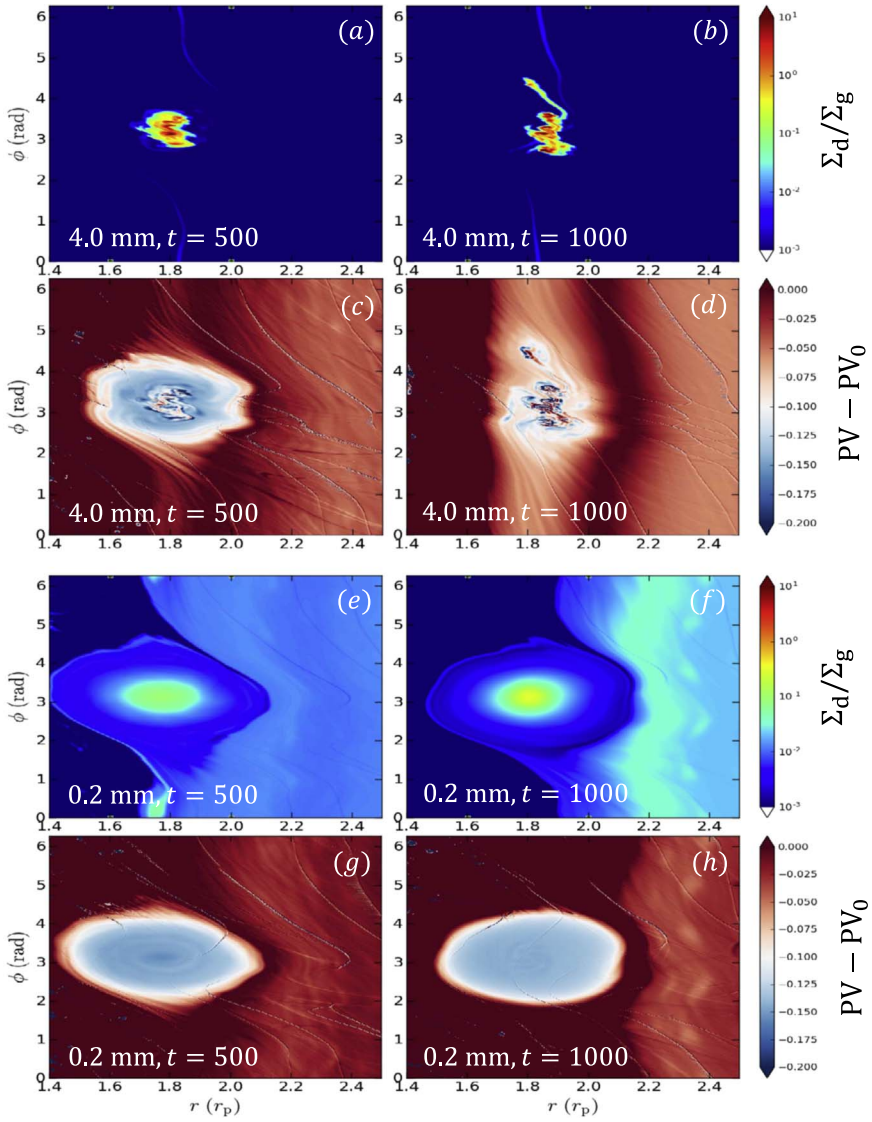

Figure 3. Σ_d/Σ_g and PV around the gaseous vortex region for the single-species runs with dust sizes of $a = 4.0$ mm (a–d) and $a = 0.2$ mm (e–h) at 500 (left panels) and 1000 (right panels) orbits.

runs as a comparison to quantify the effect of dust coagulation on the evolution of vortex. We keep all other model parameters the same except adopting a single dust size of $a = 4.0$ mm and $a = 0.2$ mm for two runs. For the case of dust size $a = 4.0$ mm, the large-scale vortex has already disappeared at ~500 orbits, as shown in Figure 3(c). The PV contour starts to become fluffy at the very early stage (e.g., before $t = 500$ orbits), and is quite turbulent at 1000 orbits, which leads to the elongation in the whole azimuthal direction. The Σ_d/Σ_g contour is quite clumpy (Figures 3(a)–(b)), which is related to the gas substructures in the same region, as indicated by the PV plot shown in Figures 3(c)–(d).

When the dust size decreases to $a = 0.2$ mm, the gas vortex can survive for a much longer time, as shown in Figures 3(e)–(h). The gaseous vortex is still quite strong, and the Σ_d/Σ_g contour is much smoother up to 1000 orbits.

The remarkable difference of the lifetime between two single-species models can also be understood from the time evolution of the dust-to-gas ratio at the vortex center shown in the lower panel of Figure 2. The collecting process for the $a = 4.0$ mm model is quite efficient compared with the coagulation run due to the absence of the initial size growth process, and also much faster than the $a = 0.2$ mm model. The latter is simply due to the large difference of dust Stokes number for two models ($\propto \mathrm{St}^{-1}$).

3.3. Dust Feedback Efficiency

We have found that the vortex lifetime in the coagulation model is in between the small and large dust runs. Since it is the efficient dust feedback process that triggers the vortex streaming instability (Surville et al. 2016), which indicates the starting point of vortex destruction by the "heavy core" instability (Chang & Oishi 2010), we plot the statistical properties in the radial band of $r \sim [1.6, 2.0]$, where the gaseous vortex is located, for several physical quantities in Figure 4, to demonstrate different feedback efficiencies in the vortex region.

When the dust coagulation is included, the distribution of Stokes number calculated using the maximum dust size[5] in

[5] The maximum dust size is approximated by the turning point in the size distribution as shown in the middle panel of Figure 2.

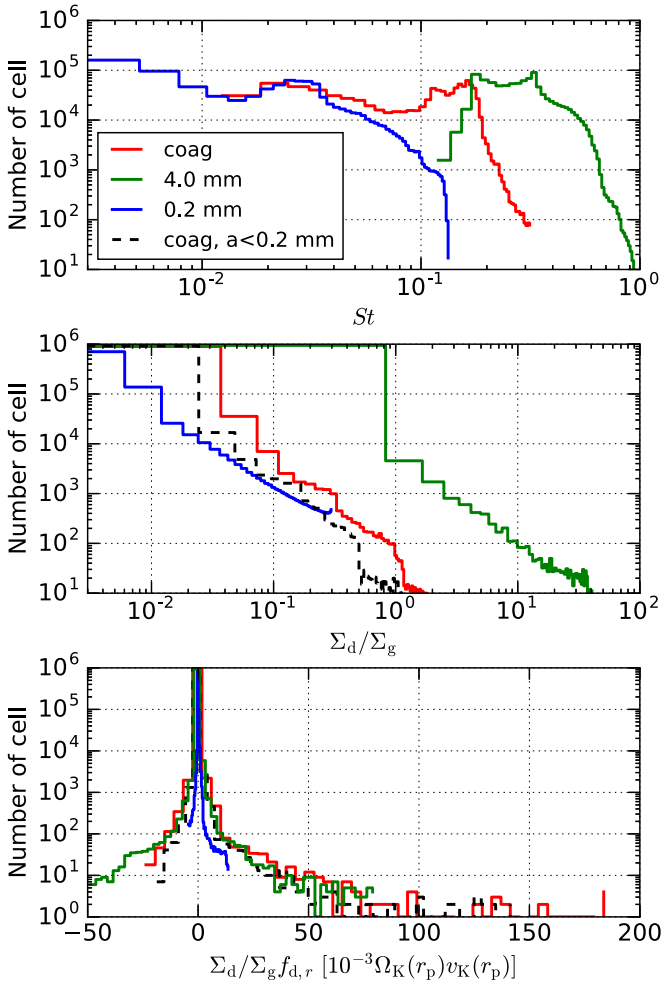

Figure 4. Histogram of different quantities with uniform binning for three runs at the region between $r \sim [1.6, 2.0]$ where the gaseous vortex is located. All these quantities are measured at 1000 orbits. Upper panel: the distribution of Stokes number. For the coagulation run, we use the maximum dust size, which is close to the turning point in the dust size distribution to calculate the Stokes number. Middle panel: $\Sigma_{\rm d}/\Sigma_{\rm g}$ distribution. Lower panel: radial feedback force $F_{{\rm d},r} = \Sigma_{\rm d}/\Sigma_{\rm g} f_{{\rm d},r}$ distribution. For the coagulation run, $F_{{\rm d},r}$ is the summation of $F^i_{{\rm d},r}$ over all dust species i. The dashed lines in the middle and lower panels show $\Sigma_{\rm d}/\Sigma_{\rm g}$ and forces contributed by small dust particles ($\lesssim$0.2 mm). We can see that small particles contribute a large fraction to the total forces.

each cell falls in between the Stokes numbers corresponding to the two single-species runs. Although most regions still have a small dust size ($\lesssim$0.2 mm) and a low Stokes number ($\lesssim$0.1) as shown in the middle panel of Figure 2, the total $\Sigma_{\rm d}/\Sigma_{\rm g}$, summed over all dust species, can be close to unity, which is much higher than that of the $a = 0.2$ mm run, even though the dust mass accumulated in the vortex region is less than that of the $a = 0.2$ mm run. This is because the vortex region, especially at its center, has a larger particle size as discussed above, that leads to an efficient collecting process into a small region within the vortex. Therefore, it is radial and azimuthal drift that delivers large particles to the vortex center, but it is the fragmentation of those particles that subsequently boosts the coupling between dust and gas by increasing the dust surface area.

We further show how this can affect the total feedback force in the vortex region. $f^i_{{\rm d},r}$ becomes a large constant of $\eta v_{\rm K} \Omega_{\rm K}$ for a small Stokes number as shown in Equation (6), which is comparable to pressure forces if $\Sigma_{\rm d}/\Sigma_{\rm g} \sim 1$. Such a large $f_{{\rm d},r}$, together with the fact that $\Sigma_{\rm d}/\Sigma_{\rm g}$ is close to unity, can contribute to strong feedback forces $\Sigma_{\rm d}/\Sigma_{\rm g} f_{{\rm d},r}$, as shown in the lower panel of Figure 4. We further find that the feedback forces from small particles with $a \lesssim 0.2$ mm contribute comparably to total forces ($\sim$70% of total forces when summed over the central tiny PV minimum region) as indicated by the dashed lines, which is due to the comparable contribution of $\Sigma_{\rm d}/\Sigma_{\rm g}$ from these small particles. Therefore, it is the high $\Sigma_{\rm d}/\Sigma_{\rm g} \sim 1$ that directly initiates the strong feedback effect and then destroys the vortex, while the large Stokes number plays the role in facilitating the increase of $\Sigma_{\rm d}/\Sigma_{\rm g} \sim 1$.

The models with only small dust as in our single-species run with $a = 0.2$ mm, even though they can have a large drag force $f_{\rm r}$ for one dust species, cannot enhance $\Sigma_{\rm d}/\Sigma_{\rm g}$ efficiently in the vortex region, and therefore result in an inefficient feedback process, shown as blue lines in Figure 4. When the dust size for the single-species run becomes much larger (i.e., $a = 4.0$ mm), $\Sigma_{\rm d}/\Sigma_{\rm g}$ increases significantly in the vortex region due to the efficient collecting process of dust, which can compensate the decrease of $f_{{\rm d},r}$ with the Stokes number, and finally leads to the strong feedback force shown in Figure 4.

3.4. Observational Implications

For the purpose of comparing with (sub)millimeter continuum observations, we utilize the `RADMC-3D` package (Dullemond et al. 2012) to produce the 1.3 and 7.0 mm dust continuum, and convolve them with a Gaussian beam of $0\farcs03 \times 0\farcs03$. The $2\,M_\odot$ star is assumed to have a blackbody temperature of 5500 K, and the disk is assumed to be at a distance of 140 pc. The details are presented in Li et al. (2019a, 2019b).

The images for different models are shown in Figure 5. When the large-scale vortex is sustained, it appears as lopsided horseshoe structures. Here we mainly focus on the long-term evolution after the destruction of the gaseous vortex (i.e., $t = 5000$ orbits, or 0.3 Myr). For the $a = 4.0$ mm run, the dust collected in the vortex is split into several hot spots at both wavelengths, while the vortex is dispersed into a remarkable ring for the $a = 0.2$ mm model (Surville et al. 2016; Surville & Mayer 2019). It is straightforward to understand that the disk is relatively brighter at the 1.33 band and dimmer at the 7.0 mm band for the smaller particle size model, as compared with another model.

For the coagulation model, two hot spots are inlaid in a dusty ring; see also the dust distribution in Figure 1. The contrast of the two hot spots becomes more remarkable at 7.0 mm due to the existence of larger particles. Note that we only have 1000 orbits for the coagulation run. To examine the long-term evolution of the structure, we include five dust species between 1.0 μm and 4.0 mm with an MRN distribution to mimic, to some extent, multiple dust species. The large-scale vortex has destroyed $\sim$2000 orbits, which is in between the two single-species runs, but still longer than that in the coagulation model due to the lack of efficient coagulation/fragmentation. The images at 5000 orbits for two bands are shown in the third column of Figure 5. We can see that the vortex appearing in the early stage will finally become a ring with some remarkable inhomogeneities at 1.33 mm. Multiple hot spots become prominent at 7.0 mm as the $a = 4.0$ mm model. It suggests that the features of hot spots inlaid within the ring are mainly related to the coexistence of both large and small particles; the

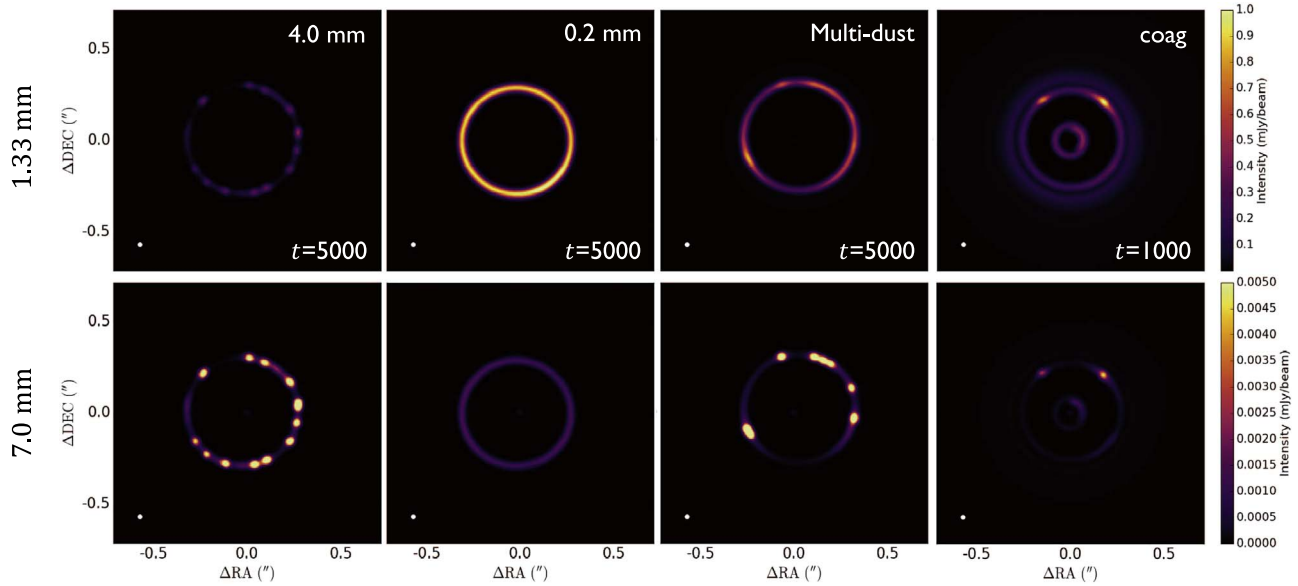

Figure 5. 1.33 mm (upper panels) and 7.0 mm (lower panels) dust continuum emission for different models (first column: 4.0 mm; second column: 0.2 mm; third column: multi-species dust; fourth column: coagulation) at 5000 or 1000 orbits indicated by the figure labels. Note that the coagulation model only has 1000 orbits due to its computational expense.

large particles appear observationally as clumpy structures, while small particles can lead to the appearance of the ring. This could have gained some observational support for the transition disk LkCa 15, which is shown as some clumpy spots at the 7.0 mm band, and appeared as a ringed structure at a shorter wavelength (Andrews et al. 2011; Isella et al. 2014).

4. Conclusions and Discussion

In this work, we perform 2D high-resolution hydrodynamical simulations with LA-COMPASS (Li et al. 2005, 2009, 2019b; Fu et al. 2014b) to study the effect of dust coagulation on the evolution of vortices induced by a massive planet embedded in a low-viscosity disk. The dust feedback has also been included to study how the dust coagulation can be effective to maintain or destroy the planet-induced vortices. We have run two single-species models with a dust size of $a = 4.0$ and 0.2 mm to compare with the full coagulation model. A multi-species run is also produced to mimic the long-term evolution of the vortex in the coagulation run.

For our coagulation model, due to the higher gas surface density and steeper pressure gradients within the vortex, dust coagulation/fragmentation and drift to the vortex center are all quite efficient, producing dust particles ranging from 1 μm to $\sim$1.0 cm, as well as overall high Σ_d/Σ_g ($\gtrsim$1). In addition, the dust size distribution is quite spatially nonuniform inside the vortex, with the Σ_d-weighted average dust size at the vortex center ($\sim$4.0 mm) being a factor of $\sim$10 larger than other vortex regions. We further find that the gaseous vortex can be destroyed within 1000 orbits of our simulations, which shows a slightly longer lifetime compared to the $a = 4.0$ mm due to the size growth process. The feedback in the coagulation model can become efficient after the total $\Sigma_d/\Sigma_g \gtrsim 1$. It is attributed to the coagulation-assisted drift and then the enhancement of the dust-to-gas ratio of small particles by fragmenting big ones, with the small particles and large ones contributing a comparable fraction to the the total feedback forces. Both of them boost the total feedback forces, which finally destroy the large-scale vortex by the vortex streaming and "heavy core" instabilities. For the single-species run with a large dust size, the effectiveness of dust feedback requires a much higher Σ_d/Σ_g by the efficient collecting of particles within the vortex.

We have examined the 1.33 and 7.0 mm dust continuum for different models after the vortex is destroyed. For the single-species run, the dusty structures are manifested as multiple hot spots or a ring depending on the dust size after the gaseous vortex is destroyed. For the coagulation and multi-dust runs, several hot spots inlaid in a ring show up in observations, contrary to single-species results, as they result from a combination of small and large particles in the ringed structure. Observational support for the coexistence of clumpy and ringed structures has been shown for transition disks (e.g., LkCa 15) at different wavelengths (Andrews et al. 2011; Isella et al. 2014).

We have not included disk self-gravity based on the initial high minimum Toomre Q ($\sim$150) for the disk we have explored. Disk self-gravity could be important for the concentrated dust after the vortex is formed. We have calculated the dust midplane density ρ_d in the vortex center region for different runs. We find that ρ_d for our coagulation run and the small dust size $a = 0.2$ mm run are about two orders of magnitude smaller than the corresponding Roche density ρ_R, which justifies the neglecting of disk self-gravity. For the larger dust size model, $a = 4.0$ mm, $\rho_d > \rho_R$. We then test this model with disk self-gravity included. It shows that it can speed up the gaseous vortex evolution, and similar dusty hot spot structures appear at the later stage.

Note that we have not explored the effect of different coagulation models, planet mass, and disk parameters on the evolution of vortices due to its computational expense. Based on our preliminary analysis, we expect a power-law disk with a shallow gas profile, which slows down the dust radial drift, could allow the gaseous vortices to survive slightly longer. A lower fragmentation velocity and a lower disk mass resulting in a smaller dust size could be helpful to sustain the large-scale vortices to a much longer time. This is because the dust feedback effect becomes weaker as the dust size gets smaller.

We have tested another single-species run with $a = 0.02$ mm, and find that the vortex can be sustained to more than 20,000 orbits, close to 1 Myr. In addition, compared to the 2D model, back-reactions are likely less efficient in 3D (Lyra et al. 2018). All of these could extend the lifetime of the gaseous vortex to ∼Myr, and explain the horseshoe structures in (sub)millimeter observations. These effect could be explored in detail in the future.

We thank the referee and Hauyu Liu for useful comments. Y. P.L., H.L., and S.L. gratefully acknowledge the support by LANL/CSES and NASA/ATP. T.B., J.D., and S.S. acknowledge funding from the European Research Council (ERC) under the European Union's Horizon 2020 research and innovation program under grant agreement No. 714769 and support from the Deutsche Forschungsgemeinschaft (DFG, German Research Foundation) through Research Unit Transition Disks (FOR 2634/1, ER 685/8-1) and under Germany's Excellence Strategy–EXC-2094–390783311. Y.P.L. thanks Daniel Carrera for helpful discussions. This research used resources provided by the Los Alamos National Laboratory Institutional Computing Program, which is supported by the U.S. Department of Energy National Nuclear Security Administration under Contract No. 89233218CNA000001.

ORCID iDs

Ya-Ping Li (李亚平) https://orcid.org/0000-0002-7329-9344
Hui Li (李晖) https://orcid.org/0000-0003-3556-6568
Shengtai Li (李胜台) https://orcid.org/0000-0002-4142-3080
Tilman Birnstiel https://orcid.org/0000-0002-1899-8783
Joanna Drążkowska https://orcid.org/0000-0002-9128-0305
Sebastian Stammler https://orcid.org/0000-0002-1589-1796

References

Andrews, S. M., Rosenfeld, K. A., Wilner, D. J., & Bremer, M. 2011, ApJL, 742, L5
Bai, X.-N., & Stone, J. M. 2013, ApJ, 769, 76
Barge, P., Richard, S., & Le Dizès, S. 2016, A&A, 592, A136
Barge, P., & Sommeria, J. 1995, A&A, 295, L1
Birnstiel, T., Dullemond, C. P., & Pinilla, P. 2013, A&A, 550, L8
Birnstiel, T., Klahr, H., & Ercolano, B. 2012, A&A, 539, A148
Calcino, J., Price, D. J., Pinte, C., et al. 2019, MNRAS, 490, 2579
Carrera, D., Gorti, U., Johansen, A., & Davies, M. B. 2017, ApJ, 839, 16
Casassus, S., van der Plas, G., M., S. P., et al. 2013, Natur, 493, 191
Chang, P., & Oishi, J. S. 2010, ApJ, 721, 1593
Crnkovic-Rubsamen, I., Zhu, Z., & Stone, J. M. 2015, MNRAS, 450, 4285
de Val-Borro, M., Artymowicz, P., D'Angelo, G., & Peplinski, A. 2007, A&A, 471, 1043
Drazkowska, J., Li, S., Birnstiel, T., Stammler, S. M., & Li, H. 2019, ApJ, 885, 91
Dullemond, C. P., Juhasz, A., Pohl, A., et al. 2012, RADMC-3D: A Multi-purpose Radiative Transfer Tool, Version 0.41, ascl:1202.015
Flaherty, K. M., Hughes, A. M., Rose, S. C., et al. 2017, ApJ, 843, 150
Fu, W., Li, H., Lubow, S., & Li, S. 2014a, ApJL, 788, L41
Fu, W., Li, H., Lubow, S., Li, S., & Liang, E. 2014b, ApJL, 795, L39
Fuente, A., Baruteau, C., Neri, R., et al. 2017, ApJL, 846, L3
Hammer, M., Kratter, K. M., & Lin, M.-K. 2017, MNRAS, 466, 3533
Huang, P., Isella, A., Li, H., Li, S., & Ji, J. 2018, ApJ, 867, 3
Isella, A., Chandler, C. J., Carpenter, J. M., Pérez, L. M., & Ricci, L. 2014, ApJ, 788, 129
Isella, A., Natta, A., Wilner, D., Carpenter, J. M., & Testi, L. 2010, ApJ, 725, 1735
Isella, A., Pérez, L. M., Carpenter, J. M., et al. 2013, ApJ, 775, 30
Klahr, H. H., & Bodenheimer, P. 2003, ApJ, 582, 869
Laune, J., Li, H., Li, S., et al. 2020, ApJL, 889, L8
Lesur, G., & Papaloizou, J. C. B. 2009, A&A, 498, 1
Li, H., Colgate, S. A., Wendroff, B., & Liska, R. 2001, ApJ, 551, 874
Li, H., Finn, J. M., Lovelace, R. V. E., & Colgate, S. A. 2000, ApJ, 533, 1023
Li, H., Li, S., Koller, J., et al. 2005, ApJ, 624, 1003
Li, H., Lubow, S. H., Li, S., & Lin, D. N. C. 2009, ApJL, 690, L52
Li, Y.-P., Li, H., Li, S., & Lin, D. N. C. 2019a, ApJ, 886, 62
Li, Y.-P., Li, H., Ricci, L., et al. 2019b, ApJ, 878, 39
Lin, M.-K., & Pierens, A. 2018, MNRAS, 478, 575
Lithwick, Y. 2009, ApJ, 693, 85
Lovelace, R. V. E., & Hohlfeld, R. G. 2013, MNRAS, 429, 529
Lovelace, R. V. E., Li, H., Colgate, S. A., & Nelson, A. F. 1999, ApJ, 513, 805
Lyra, W. 2014, ApJ, 789, 77
Lyra, W., Raettig, N., & Klahr, H. 2018, RNAAS, 2, 195
Mathis, J. S., Rumpl, W., & Nordsieck, K. H. 1977, ApJ, 217, 425
Meheut, H., Lovelace, R. V. E., & Lai, D. 2013, MNRAS, 430, 1988
Miranda, R., Li, H., Li, S., & Jin, S. 2017, ApJ, 835, 118
Muto, T., Tsukagoshi, T., Momose, M., et al. 2015, PASJ, 67, 122
Ono, T., Muto, T., Tomida, K., & Zhu, Z. 2018, ApJ, 864, 70
Pérez, L. M., Isella, A., Carpenter, J. M., & Chandler, C. J. 2014, ApJL, 783, L13
Raettig, N., Lyra, W., & Klahr, H. 2013, ApJ, 765, 115
Regály, Z., & Vorobyov, E. 2017, MNRAS, 471, 2204
Shakura, N. I., & Sunyaev, R. A. 1973, A&A, 500, 33
Surville, C., & Mayer, L. 2019, ApJ, 883, 176
Surville, C., Mayer, L., & Lin, D. N. C. 2016, ApJ, 831, 82
Takeuchi, T., & Lin, D. N. C. 2002, ApJ, 581, 1344
van der Marel, N., van Dishoeck, E. F., Bruderer, S., et al. 2013, Sci, 340, 1199
Zhu, Z., & Baruteau, C. 2016, MNRAS, 458, 3918
Zhu, Z., Nelson, R. P., Dong, R., Espaillat, C., & Hartmann, L. 2012, ApJ, 755, 6
Zhu, Z., & Stone, J. M. 2014, ApJ, 795, 53